# SAPO-34 crystals with nanosheet morphology synthesized by pyrophosphoric acid as new phosphorus source

Lei Zhao, Ge Yang, Haocheng Hu, Yuhao Sun, Zhuang Ma, Peng Peng, Eng-Poh Ng, Peng Tian, Hailing Guo, Mintova Svetlana

# SAPO-34 crystals with nanosheet morphology synthesized by pyrophosphoric acid as new phosphorus source

*Lei Zhao*[a], *Ge Yang*[a]，*Haocheng Hu*[a], *Yuhao Sun*[a], *Zhuang Ma*[a], *Peng Peng*[a],

*Eng-Poh Ng*[b], *Peng Tian*[c], *Hailing Guo*[*a], *Mintova Svetlana*[*a, d]

[a] State Key Laboratory of Heavy Oil Processing Key Laboratory of Catalysis, China National Petroleum Corp. (CNPC) China University of Petroleum (East China) Qingdao 266555, P.R. China.
[b] School of Chemical Sciences, Universiti Sains Malaysia, 11800 USM, Penang, Malaysia.
[c] National Engineering Laboratory for Methanol to Olefins, Dalian National Laboratory for Clean Energy, Dalian Institute of Chemical Physics, Chinese Academy of Sciences, Dalian 116023, China.
[d] Normandie University, ENSICAEN, UNICAEN, CNRS, Laboratoire Catalyse et Spectrochimie (LCS), 14000 Caen, France.

*Corresponding author. E-mail address: guohl@upc.edu.cn;
*Corresponding author. E-mail address: mintova@ensicaen.fr

## Abstract

The nanosheet SAPO-34 zeolite crystals with a diameter of 300 nm and a thickness of 50 nm using a new phosphorus source (pyrophosphoric acid, $H_4P_2O_7$) were synthesized. The roles of the pyrophosphate ($P_2O_7^{4-}$) species in the crystallization of SAPO-34 were elucidated. The results suggested that one P atom from the $P_2O_7^{4-}$ species participated in the formation of the CHA framework structure while the other P atom served as a crystallization control agent, facilitating preferential crystal growth in [100] crystal plane. The SAPO-34 nanosheets have silica-rich shell and phosphorus-rich core leading to superior catalytic performance in methanol-to-olefin reaction (MTO). The catalytic lifetime of the SAPO-34 nanosheets was significantly improved due to the larger amount of medium-strong surface acidity and short diffusion pathway in comparison to the conventional SAPO-34 catalyst synthesized in the presence of the classical phosphorus source ($H_3PO_4$).

**Keywords**: SAPO-34; Nanosheet; New phosphorus source; MTO

## 1. Introduction

SAPO-34 with CHA topology framework is a small pore zeotype material (pore diameter of 0.38 nm) widely applied in catalysis, and more specifically in methanol-to-olefin (MTO) process due to its excellent shape selectivity for light olefin and moderate acidity.[1–6] One of the challenges for SAPO-34 catalysts is their short lifetime due to coke formation and passivation of acid sites.[7–9] Several methods are developed toward reducing the size of crystals and/or introducing hierarchical structures of zeolite catalysts to overcome the inherent diffusion limitations and restrain bulky coke deposition.[10–15] The nanosized and hierarchical SAPO-34 catalysts showed significant enhancement of mass transfer of reactants and products, and decreased coke formation rate. However, hierarchical zeolite catalysts often sacrifice selectivity to extend lifetime.[16,17] On the other hand, the synthesis of nanosized crystals is challenging and the presence of defects may also affect the catalysts lifetime and activity.[18]

The most intuitive strategy to improve the catalytic performance of zeolites is to precisely control the morphology and elemental (Si, Al, P) distribution in SAPO-34 zeolite crystals by providing short diffusion path and more accessible active sites that can maintain both high selectivity and long catalyst lifetime. [19, 20] In this respect, Yu *et al.* synthesized SAPO-34 nanosheets (diameter: *ca.* 226 nm, thickness: *ca.* 65 nm) with different silicon contents. The results showed that the sample with the lowest silicon content (0.08) exhibited the longest catalytic lifetime exceeding 1200

min during MTO reaction.[21] Liu *et al.* reported a self-assembly method for preparation of microspherical aggregates composed of SAPO-34 nanosheets (diameter: *ca.* 50 nm, thickness: *ca.* 50 nm) using a dual templating approach ([3-(trimethoxysilyl)propyl]octadecyldimethylammonium chloride (TPOAC) and diethylamine (DEA)). The catalytic lifetime of this material displayed twice longer lifetime compared to the conventional SAPO-34.[22] Guo *et al.* reported the synthesis of SAPO-34 nanosheets with a thickness of 7 nm by re-crystallization of an ultra-thin aluminum phosphate precursor where the original lamellar morphology was preserved. These SAPO-34 nanosheets showed the highest conversion (42 %) and selectivity (74 %) in cyclohexane oxidation to adipic acid.[23] Additionally, rapeseed pollen-extract was used to prepare SAPO-34 nanosheets (thickness: 10–40 nm) with a flower-like morphology (*ca.* 10 μm) and the resulting material exhibited a high $CO_2$ adsorption capacity (2.77 mmol/g at 100 kPa) and excellent $CO_2/CH_4$ separation performance (ideal separation factor of 8.2).[24] Still the synthesis of SAPO-34 nanosheets is highly dependent on the synthesis methodology used. The crystallization mechanism, however, is not fully understood yet. In addition, the distribution of Si species together with variable diffusion path length of crystals may improve their utilization in catalysis.[25] Some strategies to modulate the location and distribution of Si species within zeolite framework by introducing surfactants,[26] crystal seeding,[27] and use of organic templates with different charge density[28] have been proposed.

Herein, we report the synthesis of SAPO-34 nanosheets using pyrophosphoric acid ($H_4P_2O_7$) as a new phosphorus source and compared to the conventional synthesis using phosphoric acid ($H_3PO_4$). In addition, the crystallization process of SAPO-34 nanosheets using $H_4P_2O_7$ was studied. Unlike the phosphoric acid, the $P_2O_7^{4-}$ resulted in slow hydrolysis, and hence interrupting the overall nucleation and crystallization processes, producing SAPO-34 crystals with nanosheet morphology and chemical gradient. The SAPO-34 crystals had P-rich inner zone and Si-rich outer zone. The SAPO-34 nanosheets exhibit high micropore volume, high specific surface area and high surface medium-strong acid sites leading to excellent performance in the MTO reaction. Furthermore, the lifetime of SAPO-34 nanosheets catalyst was 1.7 times longer than that of the conventional SAPO-34 catalyst due to low diffusion limitation and low coke formation.

## 2. Experimental section

### *2.1 Chemicals*

Phosphoric acid ($H_3PO_4$, 85 wt.%, Sinopharm), aluminum isopropoxide (98 wt.%, Alfa Aesar), aqueous silica sol (30 wt.% $SiO_2$, pH = 4.5, Sigma-Aldrich), pyrophosphoric acid ($H_4P_2O_7$, 95 wt.%, Aladdin), tetraethylammonium hydroxide (TEAOH, 25 wt.%, Aladdin), hydrochloric acid (HCl, 36–38 wt.%, Sinopharm), silver nitrate ($AgNO_3$, AR, Sinopharm) and methanol (25 wt.%, Sinopharm) were purchased and used without further purification.

*2.2 Synthesis of SAPO-34*

*2.2.1 Conventional SAPO-34*

Synthesis of conventional SAPO-34 was adopted from a recipe based on the reference [29] with some modifications. The molar composition of the synthesis gel is 3.0 TEAOH: $0.32SiO_2$: $1.0Al_2O_3$: $0.9P_2O_5$: $129H_2O$. In a typical preparation, 1.0 g of $H_3PO_4$ was first diluted in 5.0 g of double-distilled water (dd $H_2O$) before mixing with 2.0 g of aluminum isopropoxide. Then, 0.32 g of silica sol was added to the above solution followed by an addition of 8.37 g of TEAOH template to obtain a homogeneous precursor mixture. Finally, the pH value of the mixture was adjusted to 7.0 using HCl. The precursor mixture was then subjected to crystallization at 180 $^oC$ for 72 hours. The crystalline product denoted as SAPO-34-$P_1$ was subjected to purification and drying at 80 $^oC$. The occluded organic template in as-synthesized SAPO-34-$P_1$ was removed by calcination at 550 $^oC$ for 5 h in air.

*2.2.2 SAPO-34 nanosheets*

Sample SAPO-34-$P_2$ was prepared following the synthesis procedure described above but replacing the $H_3PO_4$ (1.0 g) with $H_4P_2O_7$ (1.543 g). Special attention on the hydrolysis of $H_4P_2O_7$ was paid where silver was used to detect phosphorus species anions and track the hydrolysis process of $H_4P_2O_7$ using the following assumptions: one $P_2O_7^{4-}$ could be hydrolyzed into two $PO_4^{3-}$, and $Ag^+$ reacts differently with $P_2O_7^{4-}$ and $PO_4^{3-}$ forming white or yellow precipitates, respectively. The $H_4P_2O_7$ aqueous solution with pH of 7.0 was transferred into a stainless steel autoclave and then placed

in an oven at 180 $^{o}$C for various times (0 h, 1 h, 2 h, 3 h, 4 h and 5 h). Afterwards, the $AgNO_3$ (0.88 g) was added to the samples (1 ml) subjected to various hydrolysis time. The color of the precipitates was characterized.

*2.3 Characterizations*

The phase of samples was measured using a Bruker D8 Advance alytical X'Pert Pro diffractometer with CuKα monochromatized radiation (λ = 1.5418 Å). The crystallinity of samples was calculated by integrating the corresponding XRD peaks in the 2θ range of 9°-32°. Crystallographic data of samples were obtained from powder diffraction data based on a Le Bail profile refinement and pseudo-Voigt profile function using the JANA2006 software. [30] The crystal size and morphology of solids were determined by a JEOL JSM-7900F scanning electron microscope (SEM) operating at 6 kV. Nitrogen adsorption/desorption isotherms were measured using a Quantachrome, Autosorb iQ-AG instrument. Prior analysis, the samples were activated at 300 °C for 10 hours with a heating rate 2 °C min$^{-1}$.

The chemical composition of samples was analyzed by an inductively coupled plasma atomic emission spectrometer (ICP-AES, Leeman Lab's Prodigy High Dispersion ICP instrument). Additionally, the elemental components of samples were measured by X-ray fluorescence spectrometer (XRF) using a PANalytical Axios PetroX. X-ray photoelectron spectral (XPS) analysis was carried out using a PHI 5000 Versaprobe system with a monochromatic Al Kα radiation (hν = 1486.6 eV) to determine the elemental content of crystal surface. The STEM-EDX analysis were

conducted by Thermo Fisher Scientific Talos F200x S/TEM. Thermogravimetry-Mass spectrometry (TG-MS) and Thermogravimetry differential scanning calorimetry (TG-DSC) analysis was performed using a Netzsch TG-MS (STA449 F5) instrument in the range of 40-800 °C with a ramp rate of 5 °C $min^{-1}$ in a nitrogen atmosphere.

The temperature-programmed desorption of ammonia ($NH_3$-TPD) was performed on a Micromeritics ASAP 2020C instrument. The sample (*ca.* 0.100 g) was first pretreated at 550 $^oC$ for 1 h in a He flow of 30 mL $min^{-1}$. After cooling to 70 $^oC$, the sample was saturated with 10 vol% $NH_3$/He, and then the sample was purged with He for 1 h to eliminate physically absorbed $NH_3$. Desorption of $NH_3$ was carried out under heating from 70 to 600 $^oC$ with a heating rate of 10 $^oC$ $min^{-1}$. $^{31}P$ NMR spectra were recorded on a Bruker Avance 400 (9.4 T) spectrometer using 4 mm-OD zirconia rotors and a spinning frequency of 12 kHz.

*2.4 Evaluation of SAPO-34 catalysts in methanol to olefin (MTO) reaction*

Samples SAPO-34-$P_1$ and SAPO-34-$P_2$ were tested in MTO reaction. Typically, the experiments were performed in a fixed bed reactor operating in a gas phase under atmospheric pressure. For each experiment, 800 mg of the catalyst (sieve fraction, 20-40 mesh) was loaded in the reactor and enclosed between two layers of quartz sand (20-40 mesh). The samples were activated under nitrogen flow at 550 °C for 1 hour (flow (Qv) = 90 mL $min^{-1}$) and then cooled down to the reaction temperature of 450 °C. The MTO reaction was performed with a weight hourly space velocity (WHSV) of 2.0 $h^{-1}$. The methanol vapor (60 wt.% methanol in water) was then fed in.

The methanol and related oxygenate products were analyzed by an online Agilent 6820 gas chromatograph, which was equipped with a thermal conductivity detector (TCD), while the hydrocarbon products were analyzed by an online Agilent 7820A gas chromatograph equipped with a flame ionization detector (FID).

Since the coke deposit is primarily trapped on the acid sites located in the micropore of the zeolites, the coverage of coke trapped within the deactivated SAPO-34 sample was calculated following the formula reported in [31]: $\frac{V_{Coked\ catalyst}}{V_{Fresh\ catalyst}}$ and $\frac{S_{Coked\ catalyst}}{S_{Fresh\ catalyst}}$

## 3. Results and discussion

The hydrolysis of the new phosphorus source $H_4P_2O_7$ during the synthesis of SAPO-34-$P_2$ sample was carried out under the same pH, heating temperature and time. $AgNO_3$ was selected as a probe molecule since the $Ag^+$ can react with different hydrolysates (either $P_2O_7^{4-}$ or $PO_4^{3-}$) resulting in white or/and yellow precipitates, respectively according to the following reactions:

$$4Ag^+ + P_2O_7^{4-} \rightarrow Ag_4P_2O_7 \downarrow \text{(white)} \qquad \text{(Equation 1)}$$

$$3Ag^+ + PO_4^{3-} \rightarrow Ag_3PO_4 \downarrow \text{(yellow)} \qquad \text{(Equation 2)}$$

In sample SAPO-34-$P_2$ (Supplementary Information, Fig. S1 and Table S1), the white precipitate ($Ag_4P_2O_7$) was obtained during the aging at room temperature (RT) for 2 hours (SI, Table S1, sample a). Then, the light yellow precipitate was formed under heating of the precursor at 180 $^oC$ for 1 hour due to the formation of both

$Ag_3PO_4$ and $Ag_4P_2O_7$ compounds (SI: Table S1, sample b). Upon heating at 180 $^oC$ for more than 2 hours (samples c-f), the color of precipitates changed to bright yellow due to the presence of pure $Ag_3PO_4$. The results suggest that the growth process of SAPO-34-$P_2$ crystals proceeds as follows: (a) the $H_4P_2O_7$ is ionized, resulting in the formation of $P_2O_7^{4-}$ anion at the aging stage of the precursor mixture; the $P_2O_7^{4-}$ anion reacts with the aluminate species, resulting in the formation of embryonic precursor, where one P atom in P-O-P bonds of $P_2O_7^{4-}$ takes part in the formation of crystal nucleus ; (b) the $P_2O_7^{4-}$ species is gradually hydrolyzed forming $PO_4^{3-}$ during the crystallization stage (2 hours at 180 $^oC$). More Si species enter into the framework of SAPO-34 by substituting P atoms during the crystal growth process after completion of the $H_4P_2O_7$ hydrolysis.

The crystallization process of sample SAPO-34-$P_2$ was followed by X-ray diffraction. The sharp XRD diffraction peaks at 7.6$^o$ and 9.7$^o$ 2θ corresponding to SAPO-5 and SAPO-34, respectively, are observed after two hours of hydrothermal treatment at 180 $^oC$ (Fig. 1A (b)). By increasing the synthesis time, pure SAPO-34 crystals are obtained at 24 h (Fig. 1 A (g)) with the splitting of diffraction peaks at 12.7$^o$, 15.8$^o$ and 20.4$^o$ (Fig. 1B). The evolution of crystal shape and size of sample SAPO-34-$P_2$ were studied by SEM (Fig. 2). Particles less than 10 nm are formed after 2 hours aging as shown in Fig. 2a. After hydrothermal treatment at 180 $^oC$ for 1 h, the particle size increases substantially up to 50–100 nm (Fig. 2b). After 2 hours, the particles with nanosheet morphology with a thickness of 20 nm are formed (Fig. 2c).

With the time of hydrothermal treatment prolongs to 3 hours, the thickness of crystals increases up to 30–50 nm (Fig. 2d).

The XRD patterns of samples SAPO-34-$P_1$ and SAPO-34-$P_2$ prior calcination contain Bragg peaks at 9.7°, 12.7°, 15.8°, 20.4°, 24.5° and 30.4° that correspond to pure CHA type zeolite (Fig. 3A). Besides, the diffraction peaks at 12.7°, 15.8° and 20.4° split for sample SAPO-34-$P_2$ prior calcination. In the crystallization process of sample SAPO-34-$P_2$, with the hydrolysis of the $P_2O_7^{4-}$ species, and more $PO_4^{3-}$ and Si atoms substitute the $P_2O_7^{4-}$ and participate in the framework structure with different environment of tetrahedral T sites (T = Si, Al, P). The crystallinity of samples SAPO-34-$P_1$ and SAPO-34-$P_2$ prior calcination calculated by integrating the XRD peaks at 9.7°, 12.7°, 15.8°, 20.4°, 24.5° and 30.4° is the same [32], while sample SAPO-34-$P_2$ prior calcination presents obvious preferential growth orientation along [100] crystal plane (see the Bragg peak at $2\theta$ = 9.7°). The XRD patterns of calcined samples do not change indicating their high thermal stability (Fig. 3B). Sample SAPO-34-$P_1$ prior calcination contains intergrown cubic crystals with a size of 1–4 μm (Fig. 4a). As shown in Fig. 4c, fairly uniform particles with nanosheet morphology with a length of 300 ± 50 nm and a width of 40 ± 10 nm were obtained in sample SAPO-34-$P_2$ prior calcination. The morphology and size of crystals in both SAPO-34-$P_1$ and SAPO-34-$P_2$ samples after calcination do not show obvious changes (Fig. 4b, d). The formation mechanism of nanosheets in sample SAPO-34-$P_2$ is suggested taking into account the Löwenstein's rule.[33] The P-O-P bonds do not

exist in molecular sieve framework, which means that only one P atom in $P_2O_7^{4-}$ could participate in the molecular sieve skeleton, while another P atom serves as the inert terminal tail, facilitating crystal growth towards [100] crystal plane. The unit cell parameters were determined by Le Bail refinement and pseudo-Voigt profile function (Table 1). Both unit cell parameters and volume of SAPO-34-$P_2$ are smaller than those for SAPO-34-$P_1$, inferring shorter P-O bond length in the framework of sample SAPO-34-$P_2$. [34]

The bulk chemical composition of both samples was determined by ICP-AES and XRF while the chemical composition of the crystals surface was characterized by XPS spectroscopy and the results are summarized in Table 2. The bulk Si/P ratio (determined by ICP-AES) and surface Si/P ratio (determined by XPS) of sample SAPO-34-$P_1$ are similar, i.e., 0.20 and 0.19, respectively, indicating uniform Si distribution. In contrast, a distinctive chemical distribution within the bulk and outer surface for sample SAPO-34-$P_2$ is measured. The Si/P ratios in the bulk and on the surface of sample SAPO-34-$P_2$ are 0.13 and 0.33, respectively, indicating that the Si species are mainly concentrated at the outer zone (shell) of the zeolite crystals. Scanning transmission electron microscopy energy-dispersive X-ray (STEM-EDX) analysis was performed on sample SAPO-34-$P_2$. The results are shown in Fig. 5, images were collected over areas containing agglomerates of Si and P. The outer zone of the nanosheets show an apparent higher Si/P ratio compared to the bulk (Fig.5b). This suggests that the $H_4P_2O_7$ can interfere and tune the distribution of Si species

within SAPO-34 crystals. During the initial crystallization stage, more P atoms in $P_2O_7^{4-}$ participate in the nucleation process resulting in the formation of inner P-rich zone before the hydrolysis of $H_4P_2O_7$ is complete and cannot be substituted by Si species. As a result, the Si species are forced to be bound and locate at the outer zone of the crystals, forming Si-rich surface in sample SAPO-34-$P_2$ upon completion of $H_4P_2O_7$ hydrolysis (Scheme-1).

The porosity of the samples was further studied by $N_2$ physisorption measurements. Both samples exhibit type I isotherm at low $P/P_0$ and type IV with very narrow hysteresis loop at $P/P_0$ = 0.45–0.99, indicating the typical microporous structure with small amount of mesopores (Fig. 6 and Table 3). The specific surface area, micropore volume and external surface area of sample SAPO-34-$P_1$ are 449 $m^2$ $g^{-1}$, 0.17 $cm^3$ $g^{-1}$ and 49 $m^2$ $g^{-1}$, respectively. While sample SAPO-34-$P_2$ exhibits higher specific surface area (586 $m^2$ $g^{-1}$), higher micropore volume (0.22 $cm^3$ $g^{-1}$) and similar external surface area (48 $m^2$ $g^{-1}$) to the sample SAPO-34-$P_1$.

TG-MS analysis of $CO_2$ mass signal of samples SAPO-34-$P_1$ and SAPO-34-$P_2$ prior calcination are presented in Fig. 7. As shown in Fig. 7a, the first peak at 320 $^oC$ is associated with the release of $CO_2$ coming from the occluded $TEA^+$ template in SAPO-34-$P_1$, hence indicating that the template starts decomposing at 320 $^oC$. Another template decomposition peak is located at 470 $^oC$. For sample SAPO-34-$P_2$, the first peak due to $CO_2$ release from $TEA^+$ appears at 290 $^oC$ (Fig. 7b). Four different decomposition temperatures in the TG-MS profile are also found in Fig. 6b.

Compared with two decomposition temperatures shown in the TG-MS curve of sample SAPO-34-$P_1$, sample SAPO-34-$P_2$ has four decomposition temperatures of $TEA^+$ template which may be caused by the inner and outer zones of the crystals with heterogeneous chemical composition; the $TEA^+$ template in the inner part is more difficult to be removed. As a result, the different inner and outer compositions of SAPO-34-$P_2$ crystals lead to a multi-stage decomposition of the template ($TEA^+$). The decomposition peaks located at 310 $^oC$ and 470 $^oC$ (63% $TEA^+$) represent the $TEA^+$ environment using the $PO_4^{3-}$ as the phosphorus source (outer Si-rich zone) and the decomposition peaks at 375 $^oC$ and 540 $^oC$ (37% $TEA^+$) represent the $TEA^+$ environment using $P_2O_7^{4-}$ as the phosphorus source (inner P-rich zone). As shown in Fig. 8A (b), the peak at about 430 $^oC$ in DSC curve corresponds to the major decomposition step of the template in sample SAPO-34-$P_1$. The weight loss (1.32%) of sample SAPO-34-$P_1$ before 320 $^oC$ is attributed to physically adsorbed water, while the weight loss (13.33 wt.%) between 320 and 470 $^oC$ corresponds to the decomposed organic template (Fig. 8A (a)).[35] The weight loss of 0.70% at 290 $^oC$ is attributed to physically adsorbed water, and the weight loss of 14.20% corresponds to the organic template decomposition in the sample SAPO-34-$P_2$ (Fig. 8B (a)). The amount of physically adsorbed water in SAPO-34-$P_2$ is less than that in SAPO-34-$P_1$ due to its hydrophobic Si-rich surface. The four decomposition peaks at 305 $^oC$, 375 $^oC$, 430 $^oC$ and 520 $^oC$ present in the DSC curve (Fig. 8B (b)) correspond to the different environments of the template ($TEA^+$), which is in line with the TG-MS results.

The distribution of phosphorus in the samples was evaluated by $^{31}P$ NMR spectroscopic study. The $^{31}P$ spectra of samples SAPO-34-$P_1$ and SAPO-34-$P_2$ are shown in Fig. 9. Sample SAPO-34-$P_1$ exhibits one strong peak at -28.6 ppm, which is assigned to 4-coordinated P species in the zeolite framework.[36] While sample SAPO-34-$P_2$ contains two peaks ranging from c.a. -30 to -26.7 ppm, which separately reflect four-coordinated P species originated from outer and inner zone.[37] these results are in good agreement with the TG-MS and TG-DSC results.

The acidity of samples SAPO-34-$P_1$ and SAPO-34-$P_2$ was measured by $NH_3$-TPD technique (Fig. 10 and Table 4). The peaks located in the temperature range 100–250 $^oC$ are attributed to the weak acids corresponding to P-OH, Si-OH and/or Al-OH groups that are not fully linked to $AlO_4$ tetrahedra.[38] The peaks located at temperature higher than 250 $^oC$ could be assigned to medium-strong acid site originated from bridge hydroxyl in the framework structure. The weak and medium-strong acid sites for sample SAPO-34-$P_1$ are 0.22 and 0.23 mmol $g^{-1}$, and for sample SAPO-34-$P_2$ are 0.23 and 0.19 mmol $g^{-1}$, respectively. Meanwhile, the total acid site density of samples SAPO-34-$P_1$ and SAPO-34-$P_2$ are 0.45 and 0.42 mmol $g^{-1}$, respectively. The density and strength of medium-strong acid sites of SAPO-34-$P_1$ is slightly higher than that of the sample SAPO-34-$P_2$ (Si/P =0.13) due to more Si atoms substituting the P and forming acidic site in the SAPO-34-$P_1$(Si/P =0.2), but the latter are concentrated on the surface of the crystals with Si-rich zone. The efficiency of acid active sites located on the external surface of the crystals is higher and they do

not easily form coke as previous reported.[39] As known, strong acid sites can easily promote hydrogen transfer reaction, thereby leading to rapid coke formation resulting in fast catalyst deactivation. Decreasing the acid strength and increasing the acid sites accessibility can slow down the rate of inactive carbon formation responsible for the carbon deposition, and thus extending the catalyst lifetime.

The catalytic performance of samples SAPO-34-$P_1$ and SAPO-34-$P_2$ in the MTO reaction using fix bed reactor was evaluated. As shown in Fig. 11, the initial conversion of methanol over sample SAPO-34-$P_1$ is 100% and maintained for 90 min. The conversion rapidly decreases to 80% after 120 min. The highest total selectivity of light olefin (C2–C4) is 93.7% at the conversion of 100% of methanol, where ethylene, propylene and butene selectivities are 56.1%, 30.6%, and 7.0%, respectively. On the other hand, sample SAPO-34-$P_2$ exhibits longer lifetime (150 min) compared to sample SAPO-34-$P_1$. Moreover, the coking rate is significantly slower for sample SAPO-34-$P_2$; the conversion only decreased to 80% after 270 min. The highest selectivity to light olefin (C2–C4) for SAPO-34-$P_2$ at the conversion of 100% of methanol is almost similar to the SAPO-34-$P_1$ (92.0% *vs* 93.7%). The selectivity for ethylene, propylene and butene are 57.2%, 28.8% and 6.0%, respectively. The ethylene to propylene ratio are 1.83 and 1.99 for samples SAPO-34-$P_1$ and SAPO-34-$P_2$, respectively. The coke is evenly distributed within the whole crystals of sample SAPO-34-$P_1$, while, coke is mainly trapped in the outer zone of the crystals where the acid sites of sample SAPO-34-$P_2$ are primarily located. Compared with

ethylene, the products with larger diameter like propylene and butane undergo additional diffusion resistance from the trapped coke species in the SAPO-34-$P_2$. [40] Thus the SAPO-34-$P_2$ has higher ethylene to propylene ratio selectivity. The main reasons for SAPO-34-$P_2$ with long catalytic lifetime and high selectivity for C2–C4 in the MTO reaction are as follows: (1) the introduction of $H_4P_2O_7$ as phosphorus source into SAPO-34 framework promotes the chemical composition gradient in the CHA structure with Si-rich surface and more medium-strong acid sites; (2) the crystals with nanosheet morphology with a thickness of 50 nm provide shorter diffusion path length, and thus improves molecular diffusion efficiency. It thereby inhibits the formation of polycyclic aromatic compounds; (3) the high specific surface area of the sample is favorable resulting in improved diffusion efficiency.

The feed was stopped when the conversion of methanol decreased to 80%, and the used SAPO-34-$P_1$ and SAPO-34-$P_2$ catalysts were characterized, i.e. the coke deposition and porosity were determined. The content of carbon deposition for samples SAPO-34-$P_1$ and SAPO-34-$P_2$ is 13.02 wt.% and 10.68 wt.%, respectively (Fig. S2). The porosity of the catalysts after carbon deposition was determined by $N_2$ adsorption-desorption measurement (Fig. 12 and Table S3). The remained micropore specific surface area and micropore volume of SAPO-34-$P_1$ are almost neglected. It means that the carbon deposition trapped inside the pore covers 100% of microporous surface and occupies nearly 100% micropore pore volume. In contrast, the remained specific micropore surface area and micropore pore volume of SAPO-34-$P_2$ are 78 $m^2$

$g^{-1}$ and 0.03 $cm^3$ $g^{-1}$, respectively. The carbon deposition trapped inside the pores covers 86% of surface and occupies about 86% of the micropore volume. In summary, the SAPO-34-$P_2$ shows less carbon deposits on the surface and in the pores in comparison to the SAPO-34-$P_1$.

## 4. Conclusion

In conclusion, pyrophosphoric acid ($H_4P_2O_7$) has been used as a new phosphorus source for the synthesis of SAPO-34 zeolite nanosheets. Before the completion of $H_4P_2O_7$ hydrolysis, one of the P atoms in $P_2O_7^{4-}$ species participates in the construction of CHA framework structure while the other P atom serves as the inert terminal tail, facilitating the preferential growth along [100] crystal plane. The slow hydrolysis of $P_2O_7^{4-}$ during the crystallization process results in the formation of SAPO-34 crystals with nanosheet morphology with P-rich inner zone and Si-rich outer zone. The prepared SAPO-34 nanosheets exhibit high micropore surface area and micropore volume compared to conventional SAPO-34 synthesized using $H_3PO_4$ as P source. The short diffusion path length, slow coking rate and Si-rich outer surface of SAPO-34 nanosheet crystals significantly increase their catalytic lifetime in MTO reaction while maintaining high selectivity for light olefin.

## Acknowledgements

The authors gratefully acknowledged, the National Natural Science Foundation of China (Grant No. 21975285, No. U1862118, No.21991091, No. 21991090), the Fundamental Research Funds for the Central Universities (No. 21CX06024A),

Postgraduate Innovation Projects (China University of Petroleum (East China)) (Grant No. YCX2021053), Shandong Provincial Natural Science Foundation (Grant No. ZR2021QB082), and China Postdoctoral Science Foundation (Grant No. 2021M703583).

## References

[1] C. Niu, X. Shi, F. Liu, K. Liu, L. Xie, Y. You, H. He, High hydrothermal stability of Cu-SAPO-34 catalysts for the NH3-SCR of NOx, Chem. Eng. J. 294 (2016) 254–263.

[2] J. Zhou, M. Gao, J. Zhang, W. Liu, T. Zhang, H. Li, Z. Xu, M. Ye, Z. Liu, Directed transforming of coke to active intermediates in methanol-to-olefins catalyst to boost light olefins selectivity, Nat. Commun. 12 (2021) 17.

[3] B. Gao, M. Yang, Y. Qiao, J. Li, X. Xiang, P. Wu, Y. Wei, S. Xu, P. Tian, Z. Liu, A low-temperature approach to synthesize low-silica SAPO-34 nanocrystals and their application in the methanol-to-olefins (MTO) reaction, Catal. Sci. Technol. 6 (2016) 7569–7578.

[4] G. Yang, Y. Wei, S. Xu, J. Chen, J. Li, Z. Liu, J. Yu, R. Xu, Nanosize-Enhanced Lifetime of SAPO-34 Catalysts in Methanol-to-Olefin Reactions, J. Phys. Chem. C. 117 (2013) 8214–8222.

[5] C.-Y. Di, X.-F. Li, P. Wang, Z.-H. Li, B.-B. Fan, T. Dou, Green and efficient dry gel conversion synthesis of SAPO-34 catalyst with plate-like morphology, Pet. Sci. 14 (2017) 203–213.

[6] S. Askari, R. Halladj, Ultrasonic pretreatment for hydrothermal synthesis of SAPO-34 nanocrystals, Ultrason. Sonochem. 19 (2012) 554–559.

[7] P. Peng, D. Stosic, A. Blal, A. Vimont, P. Bazin, X. Liu, Z.-F. Yan, S. Mintova, A. Travert, Unraveling the Diffusion Properties of Zeolite-Based Multicomponent Catalyst by Combined Gravimetric Analysis and IR Spectroscopy (AGIR), ACS Catal. 10 (2020) 6822–6830.

[8] P. Peng, X.-H. Gao, Z.-F. Yan, S. Mintova, Diffusion and catalyst efficiency in hierarchical zeolite catalysts, Natl. Sci. Rev. 7 (2020) 1726–1742.

[9] P. Peng, D. Stosic, X.-M. Liu, Z.-F. Yan, S. Mintova, Strategy towards enhanced performance of zeolite catalysts: Raising effective diffusion coefficient versus reducing diffusion length, Chem. Eng. J. 385 (2020) 123800.

[10] Q. Sun, Z. Xie, J. Yu, The state-of-the-art synthetic strategies for SAPO-34 zeolite catalysts in methanol-to-olefin conversion, Natl. Sci. Rev. 5 (2018) 542–558.

[11] A.Z. Varzaneh, J. Towfighi, S. Sahebdelfar, Carbon nanotube templated synthesis of metal containing hierarchical SAPO-34 catalysts: Impact of the preparation method and metal avidities in the MTO reaction, Micropor. Mesopor. Mat. 236 (2016) 1–12.

[12] G. Chen, Q. Sun, J. Yu, Nanoseed-assisted synthesis of nano-sized SAPO-34 zeolites using morpholine as the sole template with superior MTO performance, Chem. Commun. 53 (2017) 13328–13331.

[13] B. Yang, P. Zhao, J. Ma, R. Li, Synthesis of hierarchical SAPO-34 nanocrystals with improved catalytic performance for methanol to olefins, Chem. Phys. Lett. 665

(2016) 59–63.

[14] C. Wang, M. Yang, W. Zhang, X. Su, S. Xu, P. Tian, Z. Liu, Organophosphorous surfactant-assistant synthesis of SAPO-34 molecular sieve with special morphology and improved MTO performance, RSC Adv. 6 (2016) 47864–47872.

[15] X. Chen, A. Vicente, Z. Qin, V. Ruaux, J.-P. Gilson, V. Valtchev, The preparation of hierarchical SAPO-34 crystals via post-synthesis fluoride etching, Chem. Commun. 52 (2016) 3512–3515.

[16] Y. Li, S. Liu, Z. Zhang, S. Xie, X. Zhu, L. Xu, Aromatization and isomerization of 1-hexene over alkali-treated HZSM-5 zeolites: Improved reaction stability, Appl. Catal. A Gen. 338 (2008) 100–113.

[17] M.S. Holm, E. Taarning, K. Egeblad, C.H. Christensen, Catalysis with hierarchical zeolites, Catal. Today. 168 (2011) 3–16.

[18] S. Mintova, J. Grand, V. Valtchev, Nanosized zeolites: Quo Vadis?, Comptes Rendus Chim. 19 (2016) 183–191.

[19] B. Shen, X. Chen, X. Fan, H. Xiong, H. Wang, W. Qian, Y. Wang, F. Wei, Resolving atomic SAPO-34/18 intergrowth architectures for methanol conversion by identifying light atoms and bonds, Nat. Commun. 12 (2021) 2212.

[20] L. Xuan, X. Wang, Y. Zhu, Z. Li, Synthesis of low-silica SAPO-34 at lower hydrothermal temperature by additional pressure and its enhanced catalytic performance for methanol to olefin, Micropor. Mesopor. Mat. 323 (2021) 111218.

[21] Q. Sun, Y. Ma, N. Wang, X. Li, D. Xi, J. Xu, F. Deng, K.B. Yoon, P. Oleynikov, O.

Terasaki, J. Yu, High performance nanosheet-like silicoaluminophosphate molecular sieves: synthesis, 3D EDT structural analysis and MTO catalytic studies, J. Mater. Chem. A. 2 (2014) 17828–17839.

[22]C. Wang, M. Yang, P. Tian, S. Xu, Y. Yang, D. Wang, Y. Yuan, Z. Liu, Dual template-directed synthesis of SAPO-34 nanosheet assemblies with improved stability in the methanol to olefins reaction, J. Mater. Chem. A. 3 (2015) 5608–5616.

[23]X. Guo, M. Xu, M. She, Y. Zhu, T. Shi, Z. Chen, L. Peng, X. Guo, M. Lin, W. Ding, Morphology-Reserved Synthesis of Discrete Nanosheets of CuO@SAPO-34 and Pore Mouth Catalysis for One-Pot Oxidation of Cyclohexane, Angew. Chemie Int. Ed. 59 (2020) 2606–2611.

[24]J. Gong, C. Wang, C. Zeng, L. Zhang, Hydrothermal preparation of hierarchical SAPO-34 constructed by nano-sheets using rapeseed pollen extract as water and its $CO_2$ adsorption property, Micropor. Mesopor. Mat. 221 (2016) 128–136.

[25] M. Ahma, C. Cheng, P. Bhuyar, A.E. Atabani, A. Pugazhendhi, N. Chi, T. Witoon, J. Lim, J. Juan, Effect of reaction conditions on the lifetime of SAPO-34 catalysts in methanol to olefins process–A review, Fuel 283 (2021) 118851.

[26]T. Blasco, A. Chica, A. Corma, W.J. Murphy, J. Agúndez-Rodríguez, J. Pérez-Pariente, Changing the Si distribution in SAPO-11 by synthesis with surfactants improves the hydroisomerization/dewaxing properties, J. Catal. 242 (2006) 153–161.

[27]X. Wang, Z. Li, F. Gong, M. Ma, Y. Zhu, Synthesis of SAPO-34 with modifying Si distribution by seed-assisted method and its excellent catalytic performance for

methanol to olefins, Mol. Catal. 499 (2021) 111312.

[28]L. Ye, F. Cao, W. Ying, D. Fang, Q. Sun, Effect of different TEAOH/DEA combinations on SAPO-34's synthesis and catalytic performance, J. Porous Mater. 18 (2011) 225–232.

[29] Y. Cao, D. Fan, D. Zhu, L. Sun, L. Cao, P. Tian, Z. Liu, The effect of Si environments on NH3 selective catalytic reduction performance and moisture stability of Cu-SAPO-34 catalysts, J. Catal. 391 (2020) 404–413.

[30] V. Petříček, M. Dušek, L. Palatinus, Crystallographic Computing System JANA2006:General features, Z. Kristallogr. 229 (2014) 345–352.

[31] P. Magnoux, P. Cartraus, S. mignrd, M. Guisnet, Coking, Aging, and Regeneration of Zeolites, J. Catal. 106 (1987) 235-241.

[32] L. Zhao, C. Xu, S. Gao, Effects of concentration on the alkali-treatment of ZSM-5 zeolite: a study on dividing points, J. Mater. Sci. 45 (2010) 5406–5411.

[33]W. Loewenstein, The distribution of aluminum in the tetrahedra of silicates and aluminates, Am. Mineral. 39 (1954) 92–96.

[34]P.A. Jacobs, E.M. Flanigen, J.C. Jansen, H. van Bekkum, Introduction to zeolite science and practice, Elsevier, 2001.

[35]B.R. Vieira dos Santos, M. Montoya Urbina, M.J.B. Souza, A.M. Garrido Pedrosa, A.O.S. Silva, E. V Sobrinho, R. Velasco Castedo, Preparation and characterization of Pt-dealuminated Y zeolite by TG/DTA and TPR, J. Therm. Anal. Calorim. 119 (2015) 391–399.

[36]D. Hasha, L. Sierra de Saldarriaga, C. Saldarriaga, P.E. Hathaway, D.F. Cox, M.E. Davis, Studies of silicoaluminophosphates with the sodalite structure, J. Am. Chem. Soc. 110 (1988) 2127–2135.

[37]Y. Jin, Q. Sun, G. Qi, C. Yang, J. Xu, F. Chen, X. Meng, F. Deng, F.-S. Xiao, Solvent-Free Synthesis of Silicoaluminophosphate Zeolites, Angew. Chemie Int. Ed. 52 (2013) 9172–9175.

[38]W. Shen, X. Li, Y. Wei, P. Tian, F. Deng, X. Han, X. Bao, A study of the acidity of SAPO-34 by solid-state NMR spectroscopy, Micropor. Mesopor. Mat. 158 (2012) 19–25.

[39]Z. Li, J. Martínez-Triguero, P. Concepción, J. Yu, A. Corma, Methanol to olefins: activity and stability of nanosized SAPO-34 molecular sieves and control of selectivity by silicon distribution, Phys. Chem. Chem. Phys. 15 (2013) 14670–14680.

[40] H. Huang, H. Wang, H. Zhu, S. Zhang, Q. Zhang, C. Li, Enhanced ethene to propene ratio over Zn-modified SAPO-34 zeolites in methanol-to-olefin reaction, Catal. Sci. Technol. 9 (2019) 2003.

## Figures

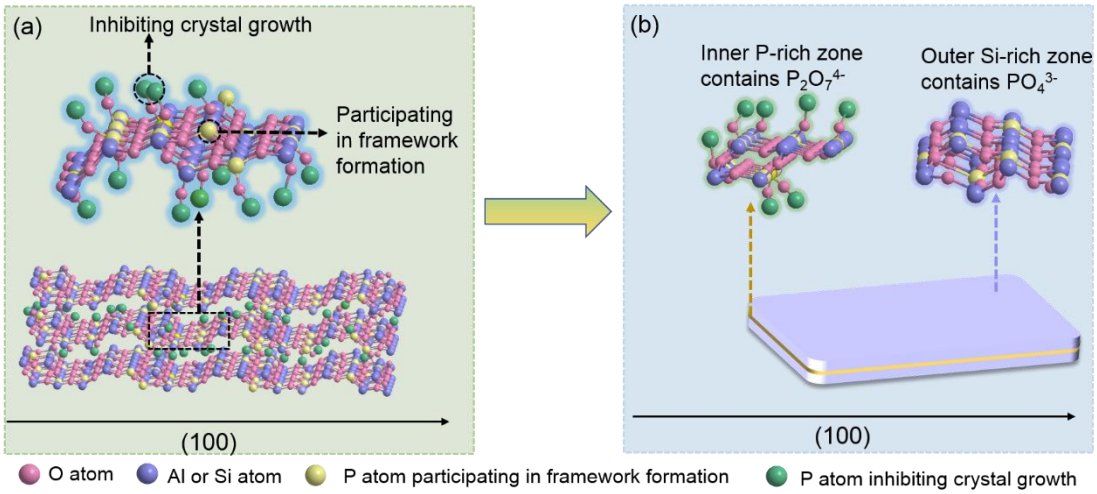


**Scheme 1**. Schematical representation of the crystal growth process of SAPO-34-$P_2$ along (100) plane: (a) one P atom participates in the framework formation (yellow balls) and the other P atom controls preferential crystal growth (green balls); (b) the inner P-rich zone contains $P_2O_7^{4-}$ and the outer Si-rich zone contains $PO_4^{3-}$ in the SAPO-34-$P_2$ structure.

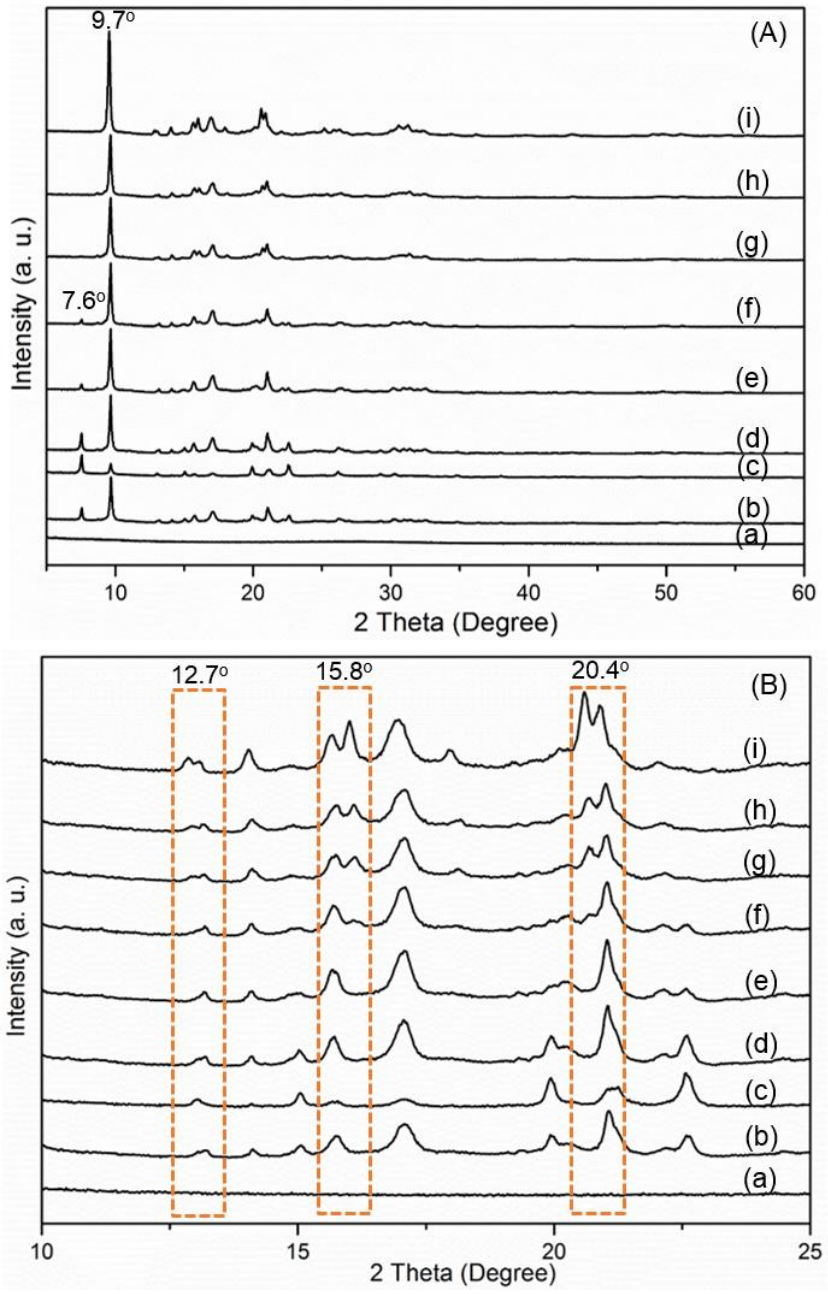


**Fig. 1** XRD patterns of sample SAPO-34-$P_2$ synthesized at 1 h(a), 2 h(b), 3 h(c), 4 h(d), 5 h(e), 12 h(f), 24 h(g), 48 h(h), 72 h(i) in the range 5–60$^o$ 2θ (A) and 10–25$^o$ 2θ (B)

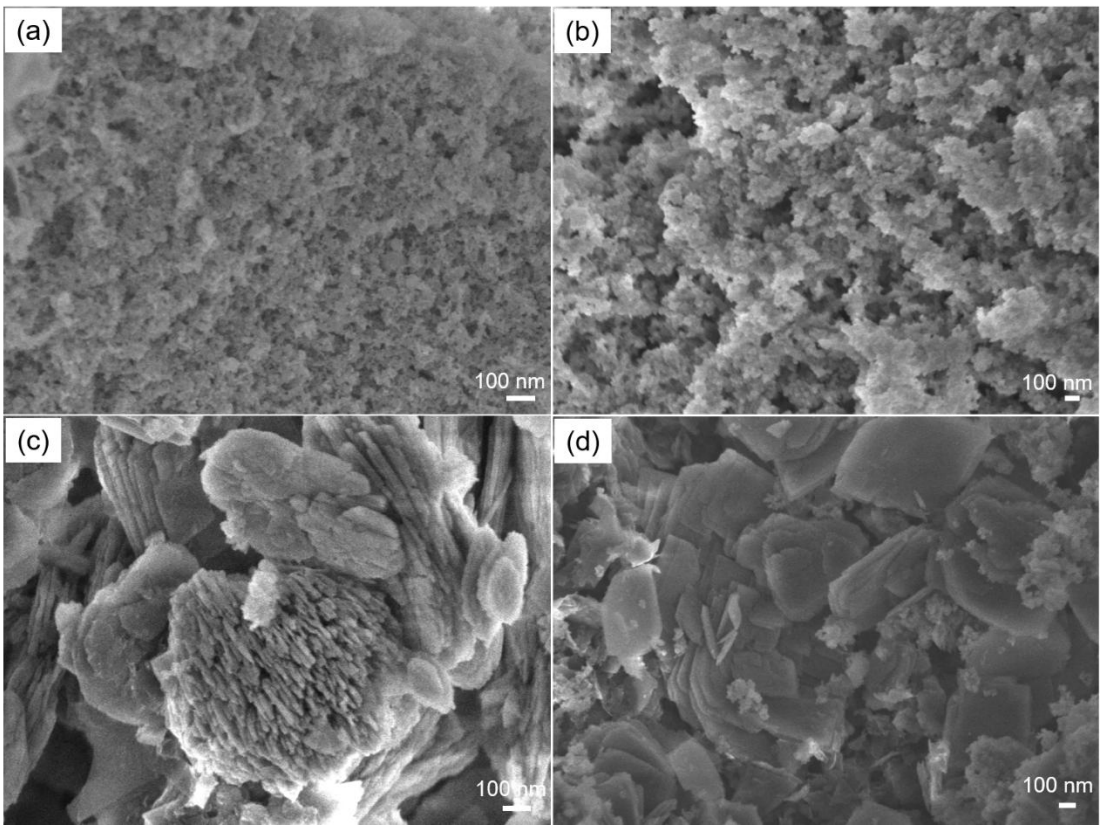


**Fig. 2** SEM pictures of samples from the series SAPO-34-$P_2$ obtained for 2 hours RT aging (a), and hydrothermal synthesis for 1 hour (b), 2 hours (c), and 3 hours (d).

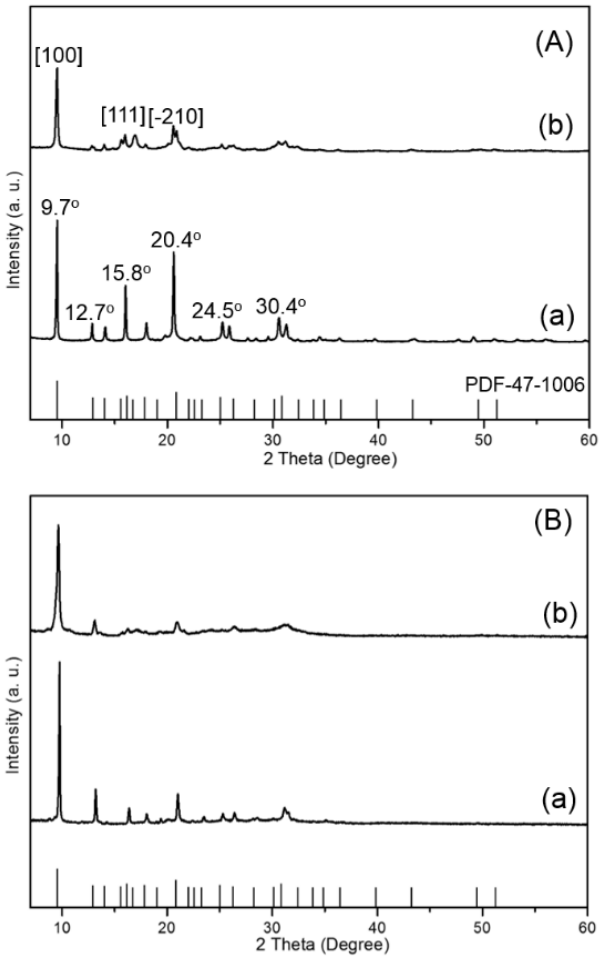


**Fig. 3** XRD patterns of sample SAPO-34-$P_1$ (a), SAPO-34-$P_2$ (b) prior calcination (A) and after calcination (B).

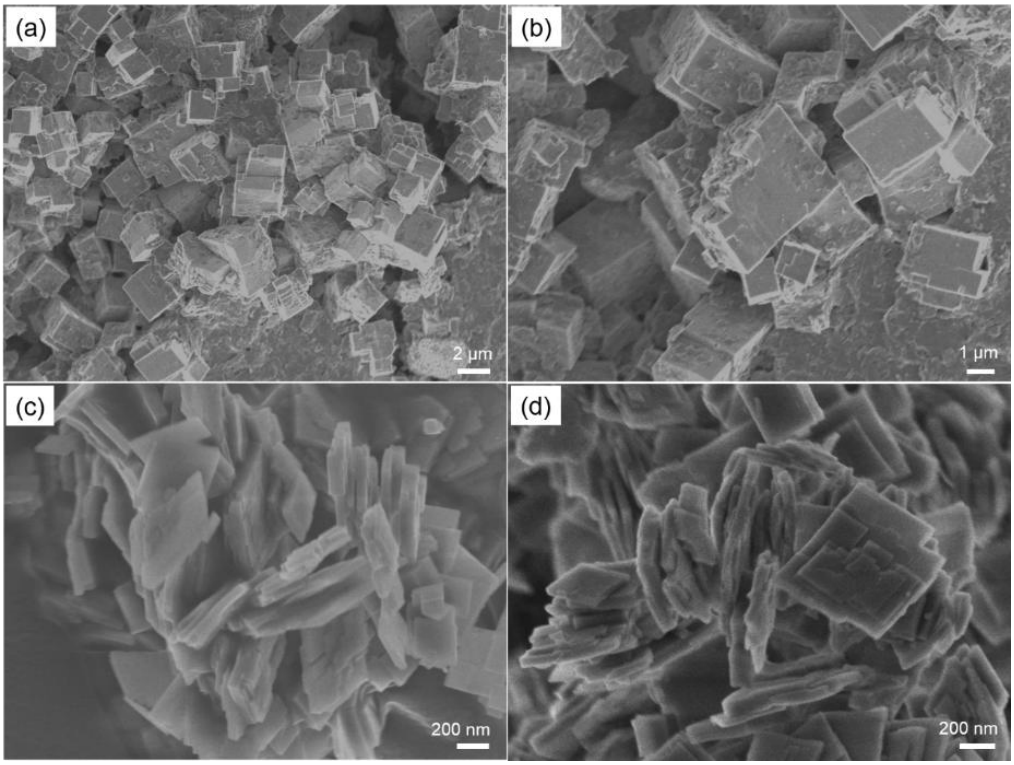


**Fig. 4** SEM pictures of sample SAPO-34-$P_1$ prior calcination (a) and after calcination (b), and sample SAPO-34-$P_2$ prior calcination (c) and after calcination (d).

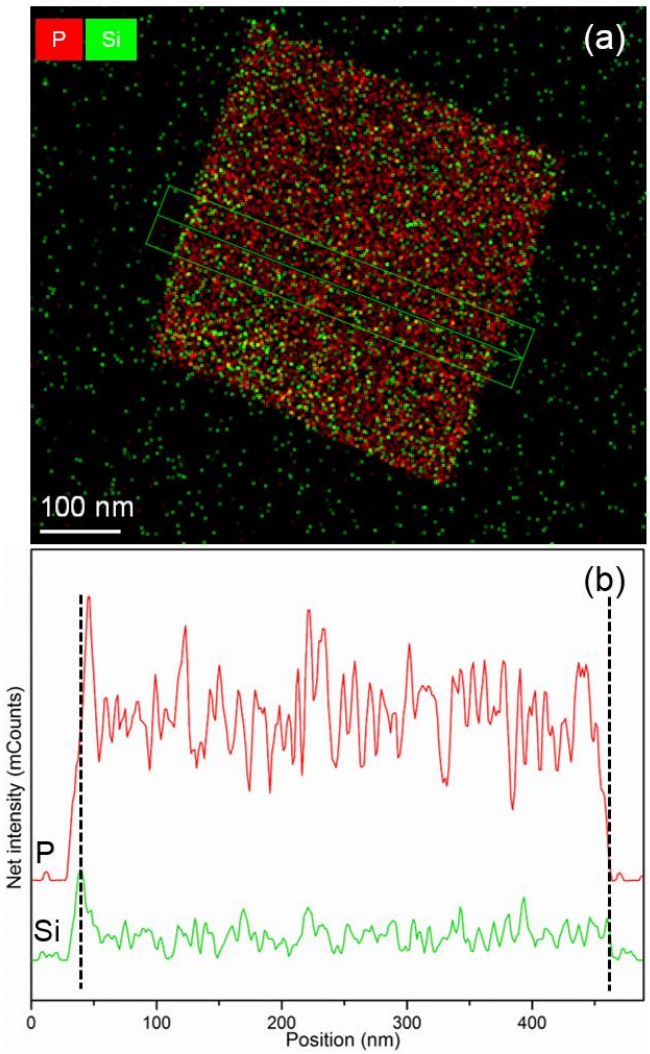


**Fig. 5** STEM-EDX elemental analysis representing the distribution of P and Si species (A) and line scan profile (B) in the sample SAPO-34-$P_2$.

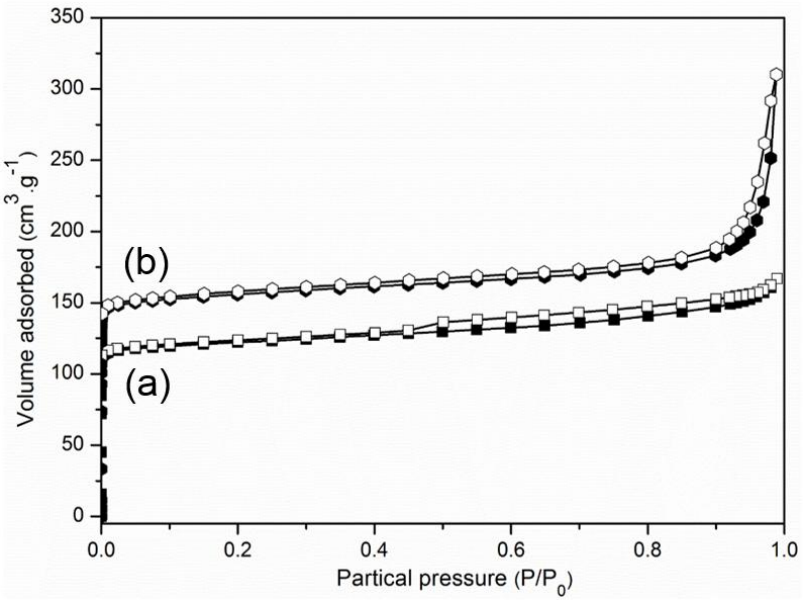


**Fig. 6** Nitrogen adsorption-desorption isotherms of samples SAPO-34-$P_1$ (a)and SAPO-34-$P_2$ (b).

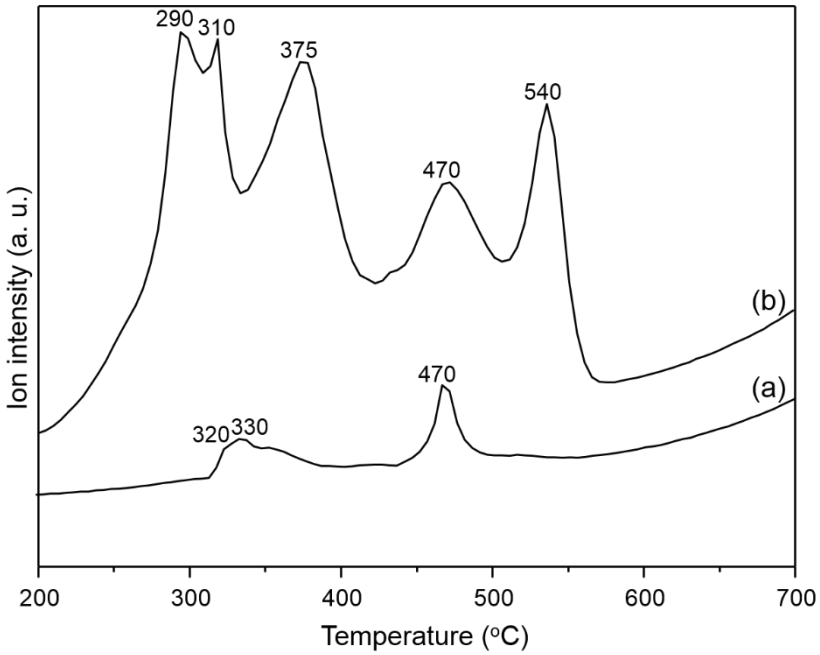


**Fig. 7** TG-MS signals of SAPO-34-$P_1$ (a) and SAPO-34-$P_2$ (b) where both lines represent molecular weight of m/z 44.

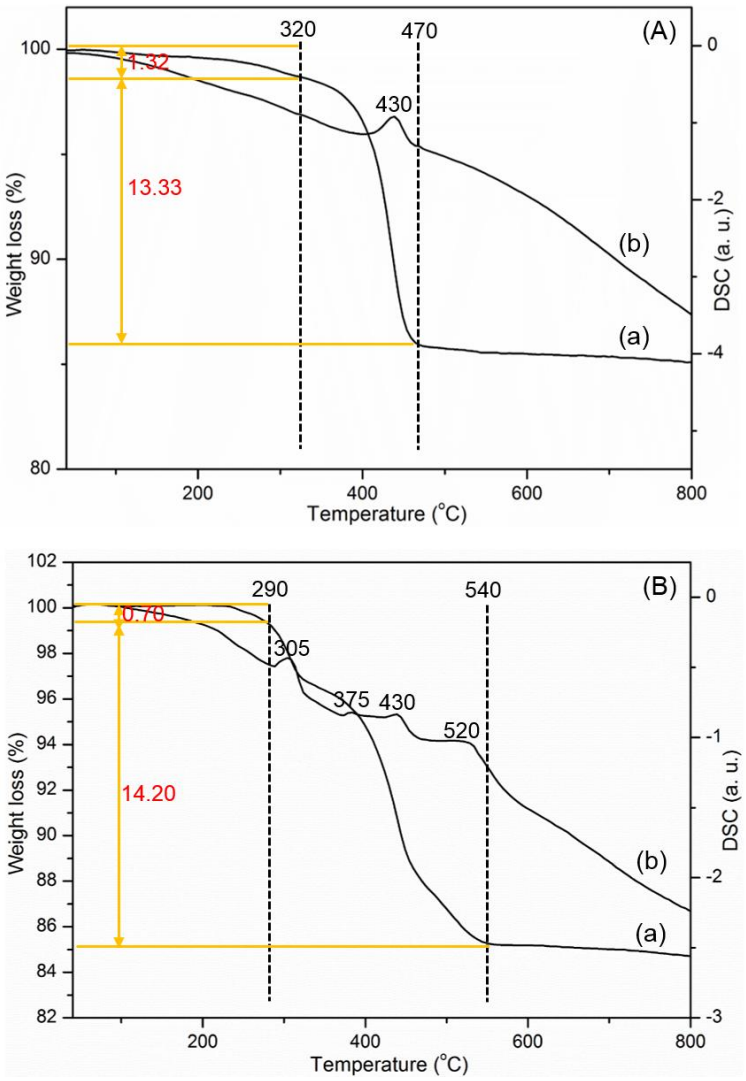


**Fig. 8** TG (a)-DSC (b) data of samples SAPO-34-$P_1$ (A) and SAPO-34-$P_2$ (B).

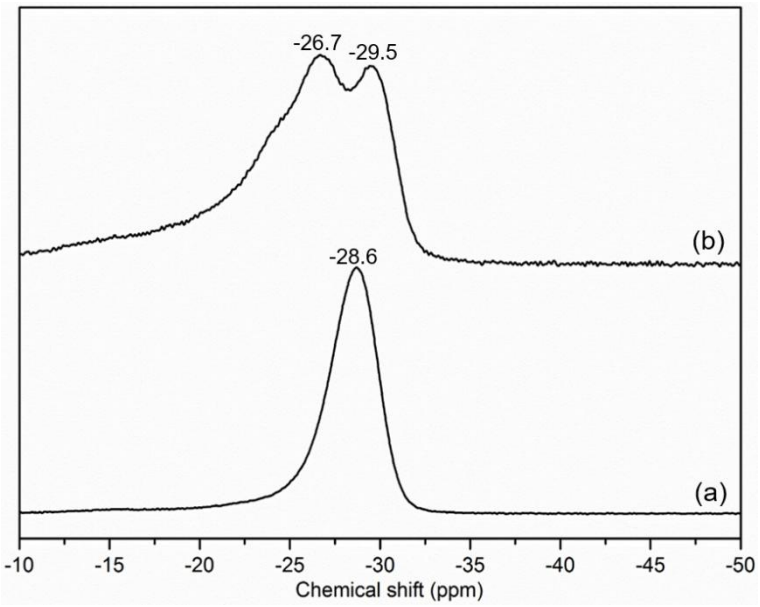


**Fig. 9** $^{31}P$ NMR spectra of samples SAPO-34-$P_1$ (a) and SAPO-34-$P_2$ (b).

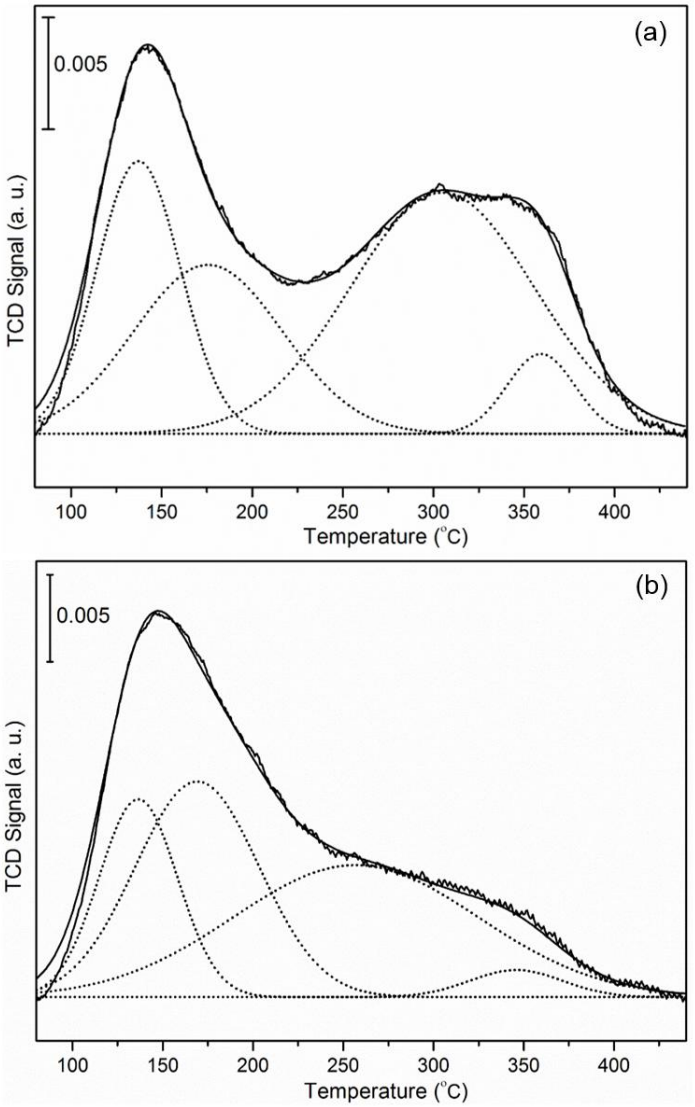


**Fig. 10** $NH_3$-TPD profiles of samples SAPO-34-$P_1$ (a) and SAPO-34-$P_2$ (b).

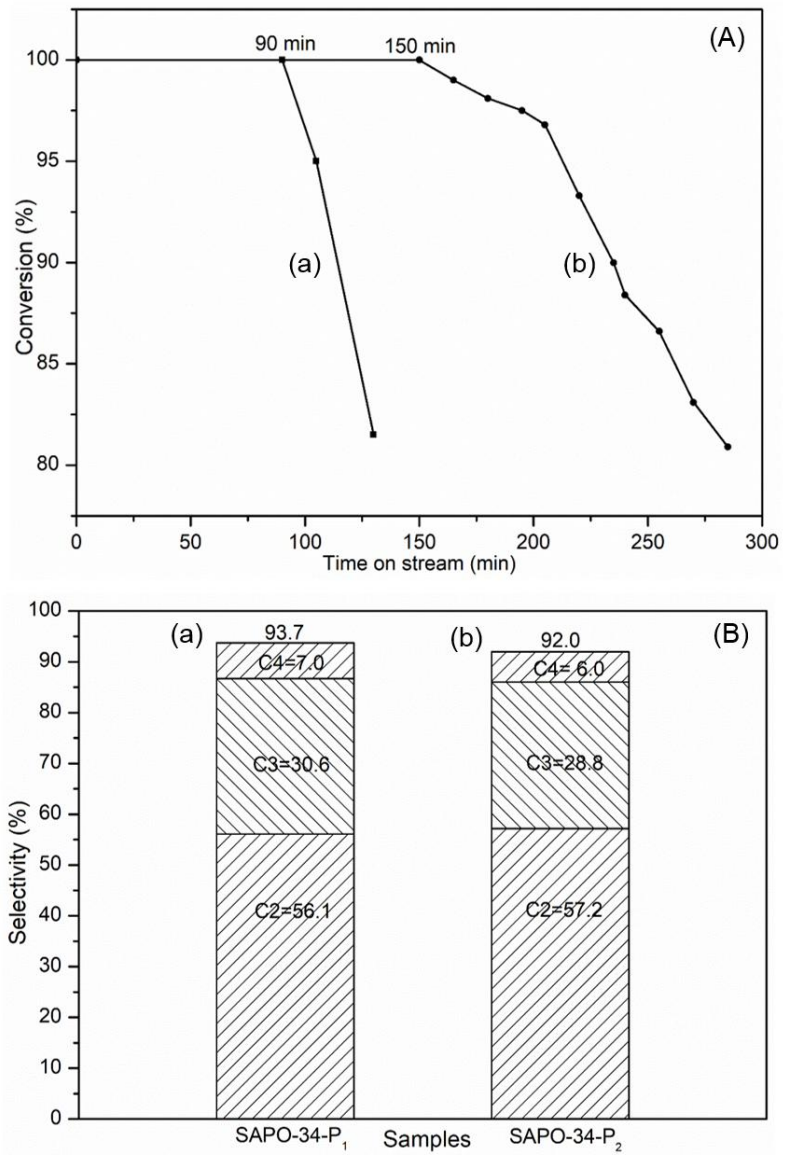


**Fig. 11** Catalytic lifetime (A) and production selectivity (B) over samples SAPO-34-$P_1$ (a) and SAPO-34-$P_2$ (b).

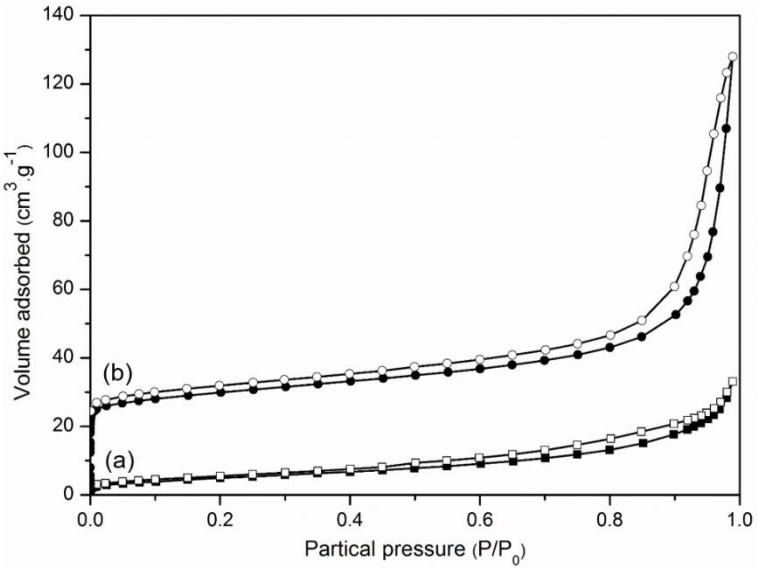


**Fig. 12** Nitrogen sorption of used catalysts containing carbon deposits: SAPO-34-$P_1$ (a) and SAPO-34-$P_2$ (b).

**Table 1** Crystallographic data of samples SAPO-34-$P_1$ and SAPO-34-$P_2$ obtained from powder diffraction data based on a Le Bail profile refinement and pseudo-Voigt profile function using the JANA2006 software.

| Samples | a (Å) | b (Å) | c (Å) | Unit cell volume (Å$^3$) | Space group |
|---|---|---|---|---|---|
| SAPO-34-$P_1$ | 13.828 | 13.828 | 14.849 | 2459.1 | R-3m |
| SAPO-34-$P_2$ | 12.662 | 12.662 | 14.011 | 2103.4 | R-3m |

**Table 2** Chemical composition of samples SAPO-34-$P_1$ and SAPO-34-$P_2$ synthesized using different phosphorus sources.

| Sample | Phosphorus source | Si/Al/P (Molar ratio ) | | |
|---|---|---|---|---|
| | | ICP | XRF | XPS |
| SAPO-34-$P_1$ | $H_3PO_4$ | 0.18:1.0:0.90 | 0.16:1.0:0.75 | 0.14:1.0:0.75 |
| SAPO-34-$P_2$ | $H_4P_2O_7$ | 0.14:1.0:1.12 | 0.12:1.0:0.90 | 0.30:1.0:0.91 |

**Table 3** Physicochemical properties of samples SAPO-34-$P_1$ and SAPO-34-$P_2$ determined from $N_2$ sorption measurements.

| Sample | $S_{BET}$ ($m^2/g$) | $S_{mic}$ ($m^2/g$) | $V_{mic}$ ($cm^3/g$) | $S_{ext}$ ($m^2/g$) | $V_{tot}$ ($cm^3/g$) |
|---|---|---|---|---|---|
| SAPO-34-$P_1$ | 498 | 449 | 0.17 | 49 | 0.25 |
| SAPO-34-$P_2$ | 634 | 586 | 0.22 | 48 | 0.48 |

**Table 4** Fit peaks location and acid sites density (ASD) ($10^{-4}$ mol $g^{-1}$) of samples SAPO-34-$P_1$ and SAPO-34-$P_2$.

| Sample | Position of peak 1 (ASD) | Position of peak 2 (ASD) | Position of peak 3 (ASD) | Position of peak 4 (ASD) | Total acid sites density (mol $g^{-1}$) |
|---|---|---|---|---|---|
| SAPO-34-$P_1$ | 137(1.04) | 175(1.14) | 304(2.03) | 359(0.24) | 4.46 |
| SAPO-34-$P_2$ | 136(0.86) | 169(1.47) | 256(1.78) | 345(0.13) | 4.25 |